



Influence of atmospheric stability on air ventilation and thermal stress in a compact urban site by large eddy simulation

Bin Lu ^{a,b}, Qiuseng Li ^{a,b,*}

^a Department of Architecture and Civil Engineering, City University of Hong Kong, Kowloon, Hong Kong

^b Architecture and Civil Engineering Research Centre, Shenzhen Research Institute of City University of Hong Kong, Shenzhen, 518057, China



ARTICLE INFO

Keywords:

Air ventilation
Thermal stress
Atmospheric stability
Urban area
Large eddy simulation

ABSTRACT

The assumption of neutral atmosphere in conventional evaluation of air ventilation and thermal stress in a compact urban area with weak wind environment may lead to errors. To assess this effect, this paper presents air ventilation and thermal stress assessment in a real subtropical urban area in Hong Kong by large eddy simulation considering stable, neutral, and unstable stratification. The air ventilation and thermal stress are measured by wind velocity ratio and Universal Thermal Climate Index, respectively. The atmospheric stabilities are quantified by vertical profiles of equivalent potential temperature based on daily radiosonde records in recent five years. The simulated results show that the conventional isothermal assumption underestimates the air ventilation capacity and overestimates the heat stress in the urban area in terms of reduced wind speeds and increased areas of strong heat stress at pedestrian-level height, respectively. The influence of urban morphology on air ventilation and thermal stress is investigated based on two urban geometry indices, namely ground coverage ratio and frontal area ratio. It is found that the ground coverage ratio is more relevant to the urban ventilation and thermal stress, but the correlations are weakened under unstable condition. On the other hand, the influence of the frontal area ratio is little. The findings of this study aim to provide a reference to the amendment of the current air ventilation assessment methodology which neglects the influence of atmospheric stability.

1. Introduction

Rapid growing populations and limited land resources are two primary causes of a global urbanization trend featuring megacities and urban agglomerations. While the congested urban configurations increase the efficiency of land and energy usage, they hinder the free flow of air inside the cities and result in weak wind environments, giving rise to several environmental issues in urban areas. Taking Hong Kong for example, the problem of limited land resources looms large to Hong Kong society as the landform is mainly peninsulas and islands dominated by hilly terrains, and only 16% of the total area is plains [1]. From 1960 to 2020, the population of Hong Kong has increased by 143% (Census and Statistics Department), and it led Hong Kong to be highly urbanized with a conglomeration of tall buildings. The high degree of urbanization has posed a significant threat to the local public health [2]. First of all, the resulting weak wind environment causes insufficient air circulation in the city, which increases the residence time of virus-laden aerosols in the air and boosts disease spread. Hong Kong was one of the hardest-hit cities in the large-scale transmission of acute respiratory

syndrome (SARS) in 2003, and it has been enduring a long period of panic of coronavirus disease (COVID-19) recently [3]. As the viruses can maintain viability in saliva aerosol particles in the air for hours [4], airborne route is an important mode of virus transmission under the weak wind environment in Hong Kong [5]. Second, urbanization is particularly relevant to extreme heat due to urban heat island effect [6, 7]. Enhanced thermal stress aggravates thermal discomfort [8] and may also be correlated to dweller mortality [9,10]. Therefore, how to reduce the environmental impacts brought by urbanization is an important research topic.

As the role of air ventilation in alleviating the above-mentioned problems is self-evident, urban air ventilation has been a rapidly expanding and enduring topic in urban planning, especially under the background of the worldwide outbreak of COVID-19 epidemic. The Hong Kong government has officially required major developments, redevelopments, and all public-funded projects to undertake the air ventilation assessment (AVA) since 2006, after being severely struck by SARS. Meanwhile, urban air ventilation-related research works have been carried out, and the area of interest ranges from street scale level

* Corresponding author. Department of Architecture and Civil Engineering, City University of Hong Kong, Kowloon, Hong Kong.

E-mail address: bcqsl@cityu.edu.hk (Q. Li).

(less than 100–200 m) to neighbourhood scale level (up to 1 or 2 km) (according to the classification by Ref. [11]). For street scale level, street canyons are considered as the basic urban form. The air ventilation in street canyons has been investigated extensively from the aspect of geometrical parameters, e.g., building aspect ratio [12–14], street width or length [15], building shape [16]. There are also some neighbourhood scale level studies related to urban air ventilation, which were mainly based on a selected site in a real urban area to investigate the influence of a target structure on the local air ventilation conditions (e.g., Refs. [17,18]).

Earlier studies about urban air ventilation were generally based on the assumption of neutral atmosphere, in which the air circulations are postulated to be purely driven by the approaching wind flows from the upstream. However, this assumption is not realistic in compact urban with weak wind environments, such as Hong Kong, where the wind flows may be dominated by buoyancy-driven convections on account of solar heating, meteorology, and anthropogenic effects [19]. According to some previous diabatic studies based on street canyons, an obvious ventilation regime transition, defined by the abrupt change of mean and turbulence quantities, can be observed when bulk Richardson number (R_b) changes the sign [20,21]. For unstable stratification, the flows are dominated by updrafts, and therefore mean and turbulent air exchange rates are found to be enhanced [22,23]. For stable stratification, the downdrafts play an important role and suppress the vertical motions of air. Therefore, the mean wind flows and turbulence may be strongly suppressed, and the pollutant retention time in the street canyon is found to be increased [24,25].

Despite the previous investigations between atmospheric stability and air ventilation, gaps in understanding the influence of atmospheric stability on urban environment remain. First of all, most previous diabatic AVA studies were based on street canyons, but only a few of them focused on real urban environments. As wind flows are different in idealized low-rise street canyon and real compact urban environment with tall buildings, the effect of atmospheric stability on air ventilation may be disparate in these two urban configurations. Second, for these diabatic AVA studies based on real urban environment [26,27], only the influence of unstable stratification on air ventilation has been discussed. As some urban observations showed that stable stratification can also occur during the daytime [28], the influence of stable stratification should also be investigated. Third, the influence of atmospheric stability on outdoor thermal stress has hardly been studied. Some earlier studies were aware of this factor in the evaluation of urban environment (e.g. Refs. [29,30]), but the relationship between atmospheric stability and outdoor thermal stress is still not clear, which results in uncertainties in urban planning. Therefore, this paper aims to fill in the research gaps and focuses on a real urban site in Hong Kong instead of an idealized urban form. Unlike previous pedestrian-level wind studies focused on strong wind conditions, this study is based on a weak wind environment which is often observed in many metropolises but was not paid much attention to in previous studies. Moreover, this study comprehensively investigates the influence of atmospheric stability on both urban air ventilation and thermal stress by large eddy simulation (LES), and major kinds of atmospheric stabilities are considered, namely stable, neutral, and unstable stratification. This paper aims to present a useful assessment framework for wind and thermal environment assessment in compact urban areas with weak wind environments.

The rest of this paper is organized as follows: the methodology of the LES is presented in Section 2. Mesh sensitivity and validation studies are given in Section 3. Air ventilation and thermal stress criteria are listed in Section 4. The influence of atmospheric stability on urban air ventilation and thermal stress and their relationship with urban morphology are presented and analysed in Section 5. Finally, the discussions and conclusions are given in Section 6 and Section 7, respectively.

2. Methodology

2.1. Selected urban site

A compact urban site in Tsuen Wan District, Hong Kong, is selected for the case study. As shown in Fig. 1 (a), the district is near a tall mountain Tai Mo Shan, which blocks the wind from the northeast. The east and south directions of the district are all typical built-up terrains with densely distributed tall buildings. The southeast direction of the district is a sea. Different atmospheric stabilities may frequently be observed during a diurnal cycle in this region as the atmosphere is likely to be unstably stratified due to anthropogenic activities at daytime and be stably stratified after sunset due to land-sea temperature difference [31].

The selected urban site is the centre of Tsuen Wan district (Fig. 1b), which has been discussed in earlier AVA studies (e.g., Refs. [32–35]). The area of interest covers a circular region with a diameter of 1200 m, and it is close to Tsuen Wan West Station (a subway station) and the sea strait Rambler Channel (Fig. 1a). Convenient transportation and panoramic view of waterfronts have attracted numerous real estate developments and resulted in a high population density. Moreover, densely distributed infrastructures, shopping malls, tall residential buildings, and schools lead to insufficient permeability and porosity in this area, and some examples are given in Fig. 1 (b). Therefore, this site can be considered as typical of a compact urban area with weak wind environment, where the influence of atmospheric stability may play an important role in local air ventilation and thermal stress.

2.2. Numerical model

The wind fields in the selected urban site are simulated using LES. The governing equations consist of continuity equation:

$$\frac{\partial \tilde{u}_i}{\partial x_i} = 0 \quad (1)$$

momentum equation:

$$\frac{\partial \tilde{u}_i}{\partial t} + \frac{\partial \tilde{u}_i \tilde{u}_j}{\partial x_j} = -\frac{1}{\rho_0} \frac{\tilde{p}}{\partial x_i} + \nu_t \frac{\partial^2}{\partial x_i^2} (\tilde{u}_i) - \frac{\partial \rho_k}{\partial x_j} g_i h_k \quad (2)$$

and temperature equation:

$$\frac{\partial \tilde{\theta}}{\partial t} + \frac{\partial \tilde{u}_i \tilde{\theta}}{\partial x_i} = \kappa_t \frac{\partial^2}{\partial x_i^2} (\tilde{\theta}) \quad (3)$$

where the tilde indicates the filtered variables. $u_i = (u, v, w)$ are the velocity components. $x_i = (x, y, z)$ are the spatial coordinates, corresponding to the streamwise, spanwise and vertical direction, respectively, and the origin is set to be the geometric centre of the selected district at the ground. p is the non-hydrostatic pressure. ν_t is air turbulent viscosity modelled by a sub-grid scale (SGS) model. This study adopts Wall-Adapting Local Eddy-viscosity (WALE) model due to its satisfactory accuracy reported in earlier air ventilation studies (e.g., Refs. [36,37]). The influence of the thermal effect on air movement is modelled by an additional buoyancy force term ($-\frac{\partial \rho_k}{\partial x_j} g_i h_k$) in the momentum equation (Eqn. (2)) based on Boussinesq approximation which assumes that temperature-induced air density change only affects the buoyancy force. The error caused by the Boussinesq approximation is less than 1% when the air temperature variation is less than 15 K [38], and therefore it is suitable for air ventilation studies. In the buoyancy term, h_k is the relative height to the ground. g is the gravity. ρ_k is the effective kinetic density and calculated by:

$$\rho_k = \frac{\rho}{\rho_0} = 1 - \beta(\theta - \theta_0) \quad (4)$$

where ρ_0 is the reference air density. θ is the equivalent potential tem-

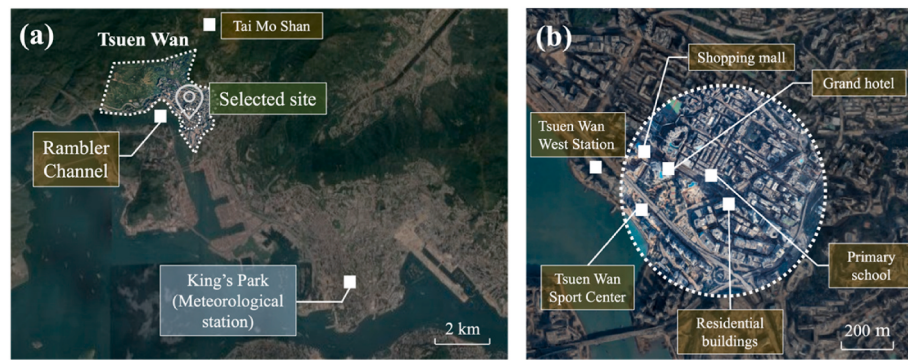


Fig. 1. Map of (a) Tsuen Wan (area enclosed by white dotted line) and (b) details of buildings in the selected urban site (area enclosed by white dotted circle), (modified from Google Maps, 2021).

perature. θ_0 is the reference equivalent potential temperature, which takes θ at the ground in this study. β is the coefficient of thermal expansion of air and takes 3.33×10^{-3} . In the temperature equation, κ_t is the turbulent thermal diffusivity calculated by ν_t/Pr_t , where Pr_t is the Prandtl number and takes 0.85.

The governing equations are solved using an open-source CFD software OpenFOAM. A second-order linear-upwind scheme is used to discretise the convective terms in the momentum and temperature equations. A second-order time scheme Crank–Nicolson is used for time-stepping. The time step size in the simulation is set as 0.2 s, and the first 2000 s is used to spin up the wind flows as it is long enough for the wind flows to cover the distance from the inlet to the outlet to initialize the flow field. The analyses in this study are based on a period of 3600 s after the spin-up time.

2.3. Computational domain

Fig. 2 shows the dimensions and boundary conditions of the computation domain. All major buildings within a diameter of 1200 m are considered. The tallest building in the target site is around $H = 250$ m, as shown in Fig. 2 (b). To save computational cost, the height of the domain is set to be $4 H$ according to previous studies related to the pedestrian-level wind comfort in the vicinity of a high-rise building [39, 40], and the lateral boundaries are $4 H$ away from the side edges of the selected urban site. These dimensions are a bit shorter than those recommended by the AIJ best practice guidelines [41], but the blockage ratio is 4.14%, which is lower than the threshold value 10% for the simulation of urban agglomerations [42]. Therefore, the blockage-induced wall effect can be neglected. The inlet is $2.4 H$ upstream from the edge of the selected urban site, and the outlet is $8.8 H$ downstream from the edge of the selected urban site to ensure that the wakes can fully develop.

The symmetry boundary condition is applied to the top and two sides of the computational domain. The outlet is set to be zero-gradient ($\partial u / \partial x = \partial v / \partial y = \partial w / \partial z = 0$). The boundary conditions of the ground and

building surfaces are set to be no-slip for wind speed. To save the computational cost, eddies near a wall are modelled by a wall function. The wall function *nutkRoughWallFunction* is adopted in this study, which incorporates the surface roughness effect into the viscous resistance prediction by setting equivalent sand-grain roughness height (k_s). The relationship between the aerodynamic roughness length (z_0) and k_s is represented by $k_s = 9.793z_0/C_s$, in which C_s is the roughness constant and typically set as 0.5 [43]. k_s of the ground is set to be 1.9 m, leading z_0 of the ground to be 0.1 m. k_s of the building surfaces is set to be 0, denoting smooth building surfaces. For the boundary condition of θ , Dirichlet boundary condition is used for the ground (equal to θ_0), and zero-gradient boundary condition is used for the building surfaces. As the Boussinesq approximation is adopted, the value of θ at the ground surface will not influence the simulation results as long as the gradient of θ is correct. Therefore, θ at the ground surface can be set as an arbitrary value in the simulation.

2.4. Mesh arrangement

The mesh scheme is created using a built-in meshing tool in OpenFOAM called snappyHexMesh, which can generate 3-dimensional (3D) hexahedra and split-hexahedra cells based on stereolithography (STL) geometry models. The STL models of the major topographies and buildings in the selected urban site are downloaded from an official map resource website managed by the Lands Department of Hong Kong Government called Hong Kong Map Services (HKMS) 2.0 (<https://www.hkmapservice.gov.hk/OneStopSystem/home>). The details of the 3D models used in this study are shown in Fig. 2 (b). For simplicity, some ignorable elements that are not regarded to substantially change the simulation results have been deleted (e.g., sparsely distributed very tiny buildings, trivial details on building facades). The general configuration of the 3D models is similar to that of a previous wind tunnel test for AVA [34], and the details of the wind tunnel test will be included in Section 3.2.

Fig. 3 shows the details of the mesh arrangement and refinements. A

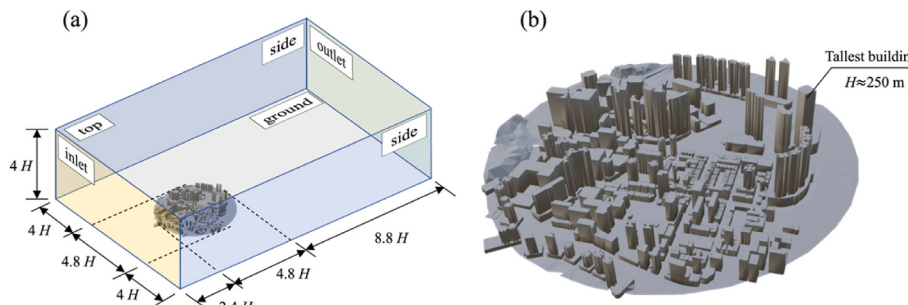


Fig. 2. Computational domain of the numerical simulation and details of the target site.

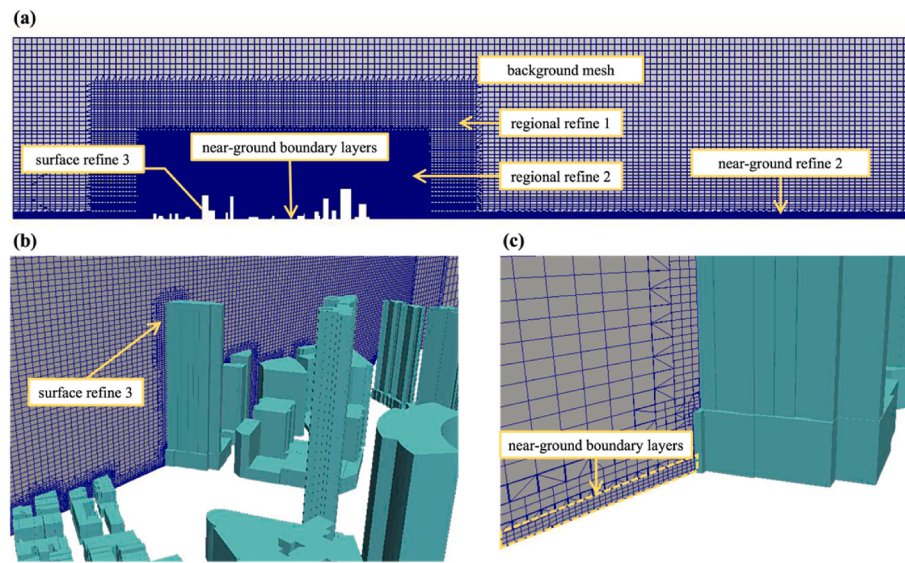


Fig. 3. (a) General mesh arrangement and refinements, and details of the mesh scheme (b) near the buildings and (c) neat the ground. Numbers in labels indicate refinement levels.

background mesh scheme is firstly created, in which no building exists, and the cells are purely hexahedra. The horizontal resolution of the cells in the background mesh scheme is $25 \text{ m} \times 25 \text{ m}$. The vertical resolution is 8 m at the ground with a small stretching factor of 1.005 to let the cell height grow vertically from the bottom to the top of the domain. Then, the meshes close to the urban site are cut by the models and refined using the snappyHexMesh tool. The refinement is quantified by “refine level”, as shown in Fig. 3. When the refinement moves up one level, the cell dimensions are reduced by half in the three orthogonal directions. As the height of interest in this study is the pedestrian-level height (2 m), the cells near the ground within the range of the selected site are particularly refined with three layers of boundary mesh, and the height of each layer is 0.6 m. It fulfills the recommendation by Blocken et al. [43]: First, the height of the cell layer closest the ground should be less than 1 m. Second, there should be at least 2 or 3 layers of cell below the pedestrian-level height. After the refinement, the cell dimensions within the range of the target site at the pedestrian-level height are $1.56 \text{ m} \times 1.56 \text{ m} \times 0.6 \text{ m}$. The validity of the current mesh scheme will be examined in Section 3.1 by a mesh sensitivity study.

2.5. Inflow conditions

2.5.1. Wind speed and turbulence profiles

Vertical profiles of mean wind speed (U), turbulence intensity (I), and turbulence integral length scale (L) at the inlet of the simulation for the validation 1 (detailed in Section 3.2.1) and main simulations are separately listed in Table 1. For the vertical profiles of U and I in the validation 1, the parameters are regressed from measured wind profiles in the wind tunnel test by Ref. [34] after scaling (the wind tunnel test was 1:400 reduced scaled, while this study performs prototype size simulations). The mean wind speed along height in streamwise direction is described by a power-law (Eqn. (5)), where z_{ref} is the reference height, U_{ref} is the mean wind speed at the reference height. Spanwise and vertical mean wind speeds are set to be zero. Turbulence intensity is assumed to be isotropic in the three orthogonal directions and adopts a logarithmic profile (Eqn. (6)).

The main simulations of this study aim to reproduce the real wind environments in Hong Kong. As is known that Hong Kong has a typical of weak wind environment, the mean wind speed measured in the urban region is around 2.5 m/s at urban canopy height [44]. This study takes $U_{ref} = 2.5 \text{ m/s}$ at $z_{ref} = 200 \text{ m}$, and the power-law exponent α adopts 0.15 for mean wind speed [40]. The profile of turbulence intensity

Table 1
Inflow wind speed and turbulence profiles for the simulations.

Variable	Type	Equation	Parameters
U	Validation 1	$U(z) = U_{ref} \left(\frac{z}{z_{ref}} \right)^{\alpha}$ (5)	$U_{ref} = 5 \text{ m/s}$ $z_{ref} = 240 \text{ m}$ $\alpha = 0.10$
	Main simulations		$U_{ref} = 2.5 \text{ m/s}$ $z_{ref} = 200 \text{ m}$ $\alpha = 0.15$
I	Validation 1	$I(z) = a - b \ln(z + z_0)$ (6)	$a = 0.172$ $b = 0.02$ $z_0 = 4.4 \text{ m}$
	Main simulations	$I(z) = I_{10} \left(\frac{z}{10} \right)^{\alpha}$ (7)	$I_{10} = 0.22$ $\alpha = -0.23$
L	Validation 1	$L_u(z) = \begin{cases} 100 & z < 30 \text{ m} \\ 100 \left(\frac{z}{30} \right)^{0.5} & z > 30 \text{ m} \end{cases}$ (8)	$\sigma_u = \sigma_v = \sigma_w$
	Main simulations	$L_v(z) = 0.5 \left(\frac{\sigma_v}{\sigma_u} \right)^3 L_u(z)$ (9)	
		$L_w(z) = 0.5 \left(\frac{\sigma_w}{\sigma_u} \right)^3 L_u(z)$ (10)	

employs that stipulated in GB50009-2012 [45] (Eqn. (7)), in which I_{10} is the turbulence intensity at 10 m height and set as 0.22, and the power-law exponent α is taken to be -0.23 for urban terrain.

For both the validation 1 and main simulations, the profiles of L adopt the recommendations in AIJ-2015 [46] in streamwise direction (Eqn. (8)) and ESDU 85020 [47] in the spanwise and vertical directions (Eqn. (9) & (10)), respectively. σ_u , σ_v , σ_w are standard deviations of wind velocity fluctuations in the three orthogonal directions, and they are equivalent due to the assumption of isotropic turbulence.

The inlet wind velocity fluctuations are generated by a synthetic turbulence generation method called the discretizing and synthesizing random flow generation (DSRFG) method proposed by Huang et al. [48]. The DSRFG method generates wind velocity fluctuations at time t by:

$$\mathbf{u}(\mathbf{x}, t) = \sum_{m=k_0}^{k_{max}} \mathbf{u}(\mathbf{x}, t) = \sum_{m=k_0}^{k_{max}} \sum_{n=1}^N \left[\begin{array}{l} \mathbf{p}^{m,n} \cos(\hat{\mathbf{k}}^{m,n} \bullet \hat{\mathbf{x}} + \omega_{m,n} t) \\ + \mathbf{q}^{m,n} \sin(\hat{\mathbf{k}}^{m,n} \bullet \hat{\mathbf{x}} + \omega_{m,n} t) \end{array} \right] \quad (11)$$

$$\text{where } \mathbf{p}^{m,n} = \frac{\xi \times k^{m,n}}{|\xi \times k^{m,n}|} \sqrt{a \frac{4E(k_m)}{N}}, \quad \mathbf{q}^{m,n} = \frac{\xi \times k^{m,n}}{|\xi \times k^{m,n}|} \sqrt{(1-a) \frac{4E(k_m)}{N}}, \quad \hat{\mathbf{x}} = \frac{\mathbf{x}}{L}, \quad \hat{\mathbf{k}} =$$

$\frac{k^{m,n}}{k_0}$, $|k^{m,n}| = k_m$, $\omega_{m,n} \in N(0, 2\pi k_m)$. \mathbf{x} represents the coordinate. $\boldsymbol{\varsigma}$ and $\boldsymbol{\xi}$ are vector forms of ς_i and ξ_i . $\varsigma_i, \xi_i \in N(0, 1)$. a is a random number uniformly distributed between 0 and 1. E indicates the target spectrum (this study chooses the von Karman spectrum). By assuming that the target spectrum is discretized into k_{max} pieces, $E(k_m)$ represents the m^{th} piece of the discretized spectrum. For each $E(k_m)$, the random fluctuating flow field is synthesized by N superpositions of harmonic functions. In this study, k_{max} takes 500 and N takes 100 according to the recommendation by Huang et al. [48]. The fluctuating wind speed profile will be superimposed to the mean wind speed profile to obtain the final time-dependent inlet wind speed profile for the CFD simulations. Fig. 4 shows the target and DSRFG-generated profiles of mean wind speed and turbulence intensity (the data points used to plot the DSRFG-generated profiles are extracted near the inlet of the CFD simulation), and the agreements are satisfactory.

2.5.2. Atmospheric stability

The temperature data recorded by an automatic weather station (1 m above the ground, 35 m above the mean sea level) in Tsuen Wan in recent five years (from 2016 to 2020) are analysed first. The hottest months in Hong Kong are July and August in summer with mean temperature at the pedestrian-level height reaching 27 °C. As the weak wind environment in Hong Kong often results in a lack of air ventilation and severe thermal discomfort to the citizens in summer, July and August are the target months for the subsequent analyses in this study.

The atmospheric stability conditions can be obtained based on the daily records of θ at 00:00 and 12:00 in Greenwich Mean Time (corresponding to 08:00 and 20:00 in Hong Kong local time) at King's Park meteorological station (KP). Its records are available on the website managed by the Department of Atmospheric Science, University of Wyoming (<http://weather.uwyo.edu/upperair/sounding.html>). The location of KP is denoted in Fig. 1, which is around 9 km away from the target site. Hence, it reveals the limitation that the atmospheric stability conditions at KP may not be exactly consistent with those in the target region due to different local environmental situations or factors, such as topography and vegetation. However, this study chooses the temperature data recorded at KP to analyse the atmospheric stability for two reasons: 1. KP is the closest meteorological station to the target site whose measured vertical profiles of θ are available to the public. 2. The analyses of the vertical profiles of θ only intend to obtain a reasonable

range of vertical gradient of θ which can qualitatively reflect the atmospheric stability conditions in a typical compact urban environment in Hong Kong. Therefore, the potential different atmospheric stability conditions in the target site and KP caused by local environmental factors will not substantially influence the conclusions of this study.

The records of θ data were measured by radiosonde balloons at different observation heights h (observation height means the height relative to the ground of King's Park). Values of θ are assumed to vary linearly between two adjacent observations heights, and accordingly the gradient of θ ($d\theta/dh$) at any observation height can be calculated. All the measured vertical profiles of θ (radiosonde balloons are released twice per day by Hong Kong Observatory, two profiles can be obtained every day) in July and August from 2016 to 2020 are analysed, and the obtained boxplots of $d\theta/dh$ at different heights are shown in Fig. 5. The mean values of all positive and negative $d\theta/dh$ are calculated, and they are equal to 0.006 and -0.011 K/m, respectively. Because both stable and unstable conditions were frequently observed, they are all considered in the simulations of this study.

Although there were comprehensive studies on wind profiles within urban areas (e.g. Refs. [49,50]), relatively less information on representative temperature profiles in urban areas is available. Therefore, this study postulates linear θ profiles as the initial conditions and the inlet temperature profiles to mimic atmosphere stratifications:

$$\theta(z) = \theta_0 + \frac{d\theta}{dz}z \quad (12)$$

This assumption was also made in the previous studies related to diabatic urban flows based on a street canyon [22] or an isolated tall building [51], and linear θ profiles can also be observed in the radiosonde records (not shown here). As mentioned in Section 2.3, the setting of θ_0 does not influence the simulated results under the Boussinesq approximation, but it is crucial in evaluating thermal stress as θ is related to temperature (T). Therefore, θ_0 can be an arbitrary value in the simulation. However, after the simulation, one needs to add an appropriate value to the whole θ field (i.e., add a same value to all the cell values of θ) to let the derived space- and time-averaged T at the pedestrian-level height be consistent with that in the field observation (space- and time-averaged T at the pedestrian-level height is 27.3 °C according to the measured mean temperature in recent five years by the automatic weather station in Tsuen Wan).

For the stable case, $d\theta/dz$ in the simulation is set to be the mean value

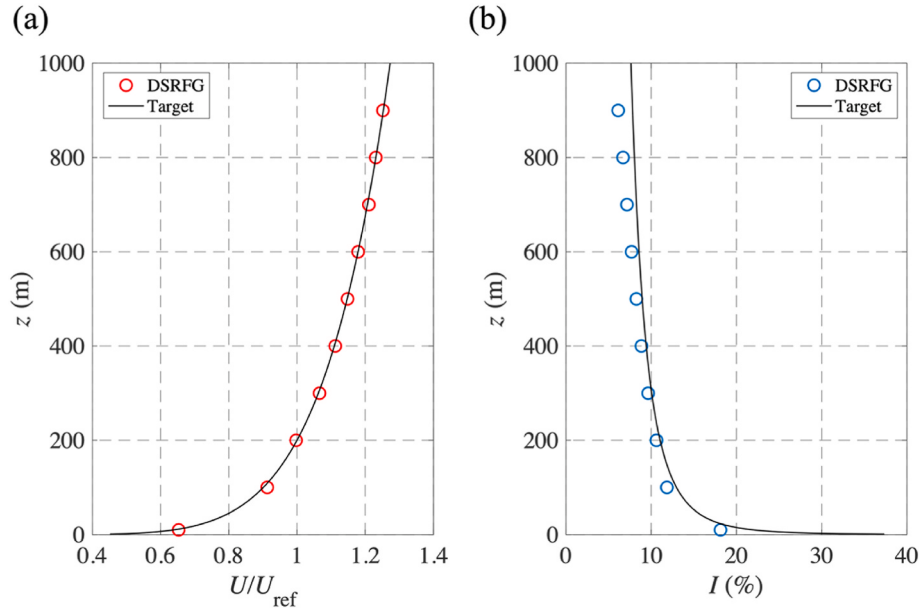


Fig. 4. Comparison of the target and DSRFG-generated profiles of (a) mean wind speed and (b) turbulence intensity.

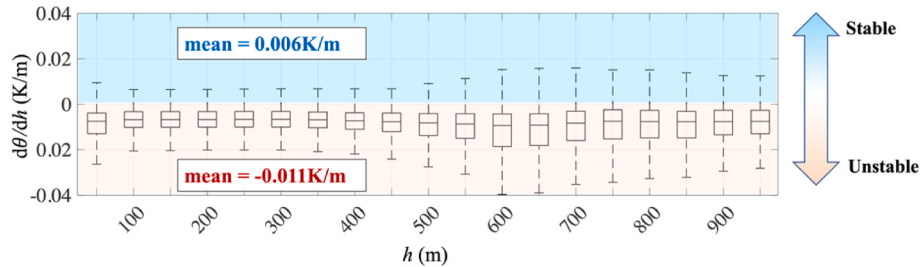


Fig. 5. Boxplot of gradient of θ at different observation heights based on daily radiosonde measurements at King's Park in July and August from 2016 to 2020.

of all positive $d\theta/dh$ in Fig. 5, namely 0.006 K/m, for the initial condition and the inlet profile of θ . For comparison purpose, $d\theta/dz$ is taken to be -0.006 K/m for the unstable case. As for the neutral case, $d\theta/dz$ is set to be 0 K/m.

3. Mesh sensitivity and validation studies

3.1. Mesh sensitivity study

A mesh sensitivity study is carried out under the neutral condition using three mesh schemes with different mesh resolutions labelled Coarse, Medium, and Fine mesh, respectively, to ensure the simulated results are independent of the mesh spatial resolution. The dimensions of the cells in the Medium mesh scheme has been described in Section 2.4. The Coarse mesh and Fine mesh schemes employ a length factor of 1.5 in the two horizontal directions to coarsen and refine the horizontal mesh resolution of the background mesh in the Medium mesh scheme, respectively, as shown in Fig. 6. The settings of snappyHexMesh are generally the same in all the cases and follow the illustrations in Section 2.4, but some details are slightly adjusted in different cases to prevent the appearance of highly skewed cells, such as local refinements at some corners. Finally, the total cell numbers in the Coarse, Medium, and Fine mesh schemes are 4.49 million, 7.44 million, and 19.9 million, respectively. The one with acceptable computational cost and desirable accuracy will be chosen for the validation 1 and main simulations in this study. The mesh sensitivity is evaluated by comparisons of root-mean-square-error (RMSE) using normalized wind speed (K) extracted at selected points in any two mesh schemes:

$$K = \frac{\bar{u}_p}{\bar{u}_{\text{ambient}, p}} \quad (13)$$

$$\text{RMSE} = \sqrt{\frac{1}{N_i} \sum_{i=1}^{N_i} (K_{1,i} - K_{2,i})^2} \quad (14)$$

where \bar{u}_p is the mean wind speed at the pedestrian-level height (2 m) at a selected point when existing buildings are considered, and $\bar{u}_{\text{ambient}, p}$ is the corresponding mean ambient wind speed at the same point without the buildings. $K_{1,i}$ and $K_{2,i}$ represent the normalized mean wind speeds extracted at the i^{th} selected point in two mesh schemes. N_i is the total

number of the selected points. As the area of the target site is large and building configurations are complicated, only the K values of the two major roads crossing through the area of interest are extracted to show a clearer comparison, as denoted in Fig. 7 (a), and the sampling distance is set to be 15 m.

Fig. 7(b)–(d) show comparisons of K among the three mesh schemes. The comparisons of K in Coarse – Medium and Coarse – Fine mesh show that a large portion of data is located outside 20% error lines. As for the comparison of Medium – Fine mesh, though there are few outlier points with relatively large errors, most data points are bounded by the 20% error lines and closer to 0% error line compared to the other comparisons. The RMSE value of Medium – Fine mesh is also much lower than those in other comparisons. Therefore, the simulated results by using the Medium mesh scheme is considered to be grid independent. To balance the accuracy and computational cost, the Medium mesh scheme is used for the validation 1 and main simulations in this study.

3.2. Validation

The validation of this study is divided into two parts, namely validation 1 and validation 2. The validation 1 focuses on the accuracy of the CFD model in simulating complex urban flow under neutral stratification. The validation 2 focuses on the effectiveness of the CFD model when different stratifications are considered.

3.2.1. Validation 1: CFD model of urban flow under neutral stratification

Wind tunnel test results by Ref. [32] are used to validate the CFD model in simulating complex urban flow under neutrally stratified condition. The wind tunnel test was conducted in a closed-return type boundary layer wind tunnel (BLWT) at Hong Kong University of Science and Technology (HKUST) with 5 m wide and 4 m high, and the geometric scale ratio of the building models was 1:400. The building models used in the wind tunnel test are shown in Fig. 8 (a), and the selected points used for the validation are denoted in Fig. 8 (b). The comparison of K at the selected points between the wind tunnel test and the present CFD simulations are plotted in Fig. 8 (c). The comparison shows a quantitatively good agreement for most data (56% CFD data located in the 20% error lines, and 70% in the 40% error lines). The points with large errors are most likely to be caused by the mismatch of the building models downloaded from HKMS 2.0 and those in the wind tunnel test.

The difference of K between the CFD simulation and the wind tunnel

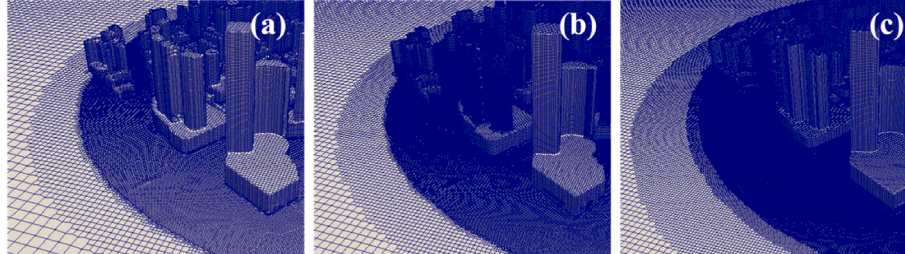


Fig. 6. Details of (a) Coarse mesh, (b) Medium mesh, and (c) Fine mesh.

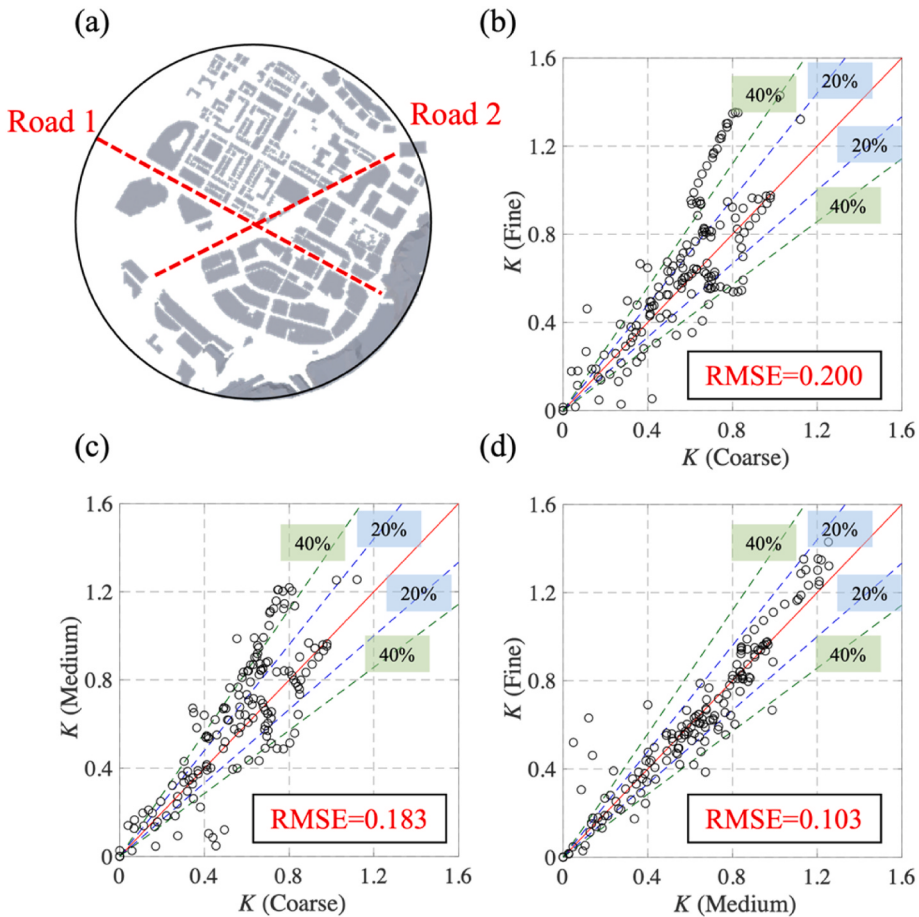


Fig. 7. (a) Two major roads considered for sensitivity test, and comparison of K in (b) Coarse – Fine mesh, (c) Coarse – Medium mesh, and (d) Medium – Fine mesh.

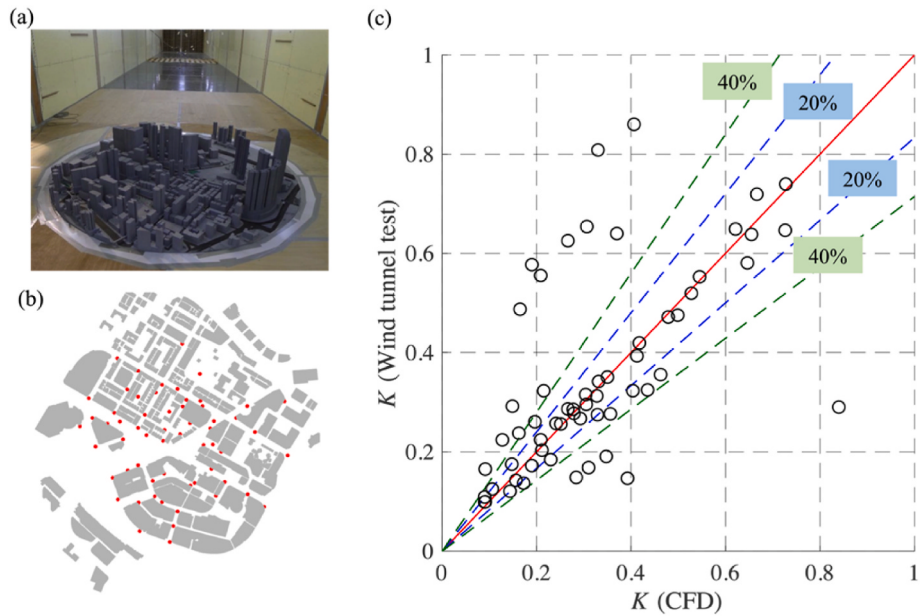


Fig. 8. (a) Urban models in the wind tunnel test [32], and (b) selected points for validation (red dots). (c) Comparison of K at the selected points between the wind tunnel test and CFD simulation. (For interpretation of the references to colour in this figure legend, the reader is referred to the Web version of this article.)

test is further quantified by validation matrices. Three indices are adopted in this study: Normalized Mean Square Error (NMSE), Frictional Bias (FB), and Pearson Correlation (R):

$$\text{NMSE} = \frac{\sum_{i=1}^{N_i} (C_i - W_i)^2}{\sum_{i=1}^n (C_i W_i)} \quad (15)$$

$$FB = \frac{\bar{C} - \bar{W}}{0.5(\bar{C} + \bar{W})} \quad (16)$$

$$R = \frac{\sum_{i=1}^{N_i} [(C_i - \bar{C})(W_i - \bar{W})]}{\sqrt{\sum_{i=1}^{N_i} (C_i - \bar{C})^2} \sqrt{\sum_{i=1}^{N_i} (W_i - \bar{W})^2}} \quad (17)$$

where the overbar indicates the average over all the data in C or W . C and W represent K values in the CFD simulation and wind tunnel test, respectively. The calculated values of the validation matrices are listed in Table 2. The ideal values and criteria of these validation matrices can be found in Schatzmann et al. [52], and they are also listed in Table 2. By comparison, NMSE and FB meet the criteria. However, R is lower than the expected threshold, which should be attributed to the existence of some outlier points shown in Fig. 8 (c). Considering the complexity of urban flows and the differences between the building models in the wind tunnel test and those in the CFD simulation, the errors are acceptable.

3.2.2. Validation 2: CFD model under stable and unstable stratification

Most non-isothermal urban flow studies to date conducted by diabatic wind tunnel tests focused on idealized building arrays by ground heating or cooling. Therefore, the CFD model of this study is validated against a diabatic wind tunnel test conducted by Uehara et al. [53] to ensure that the buoyancy forces and temperature distributions are correctly modelled. The computational domain is shown in Fig. 9 (a), in which both the rough upwind fetch section and the test section of the wind tunnel test are considered. The upwind fetch section contains a H_c high tripping fence and an array of $H_c \times H_c \times H_c/2$ roughness elements spaced H_c apart on all sides, where H_c is the height of the cube models in the test section. In both sections, the cell size of the mesh is $H_c/10 \times H_c/10 \times H_c/10$, and the cells near the ground are refined with 15 layers of boundary mesh with a stretching factor of 1.3 to capture more near-ground flow features. The boundary conditions are generally the same as those described in Section 2.3, but the two lateral sides are set to be cyclic, and the ground is set to be a smooth wall ($z_0 = 0$ m).

The stratifications in the test section are created by ground cooling and heating and described by a nondimensional parameter bulk Richardson number (R_b), which is calculated by:

$$R_b = \frac{\left(\frac{g}{T} \frac{T_{H_c} - T_0}{H_c} \right)}{\left(\frac{U_{H_c}}{H_c} \right)^2} \quad (18)$$

where g is the gravitational acceleration. T_{H_c} and U_{H_c} are the temperature and wind speed at height of H_c , respectively. T_0 is the temperature close to the ground level ($z = 0.002H_c$). \bar{T} is the mean canyon temperature. In the original wind tunnel test, the difference between T_{H_c} and T_0 can exceed 15 K in most cases, and therefore Boussinesq approximation cannot be directly applied to model the buoyancy force. To solve this problem, the value of H_c is scaled in the simulation to let the difference between T_{H_c} and T_0 be less than 15 K under the similarity of R_b (H_c is finally taken to be 10 m, and the length scale ratio is 1:100). It should be noted that T_0 , T_{H_c} , and \bar{T} are not known before the simulations, and hence the value of ground temperature should be adjusted in an iterative manner to let R_b in the simulation close to that in the wind tunnel test. However, exact match of R_b in the simulation and that in the wind tunnel test is not guaranteed.

The upwind fetch section and the test section are simulated

Table 2
Validation matrices, including the ideal values, criteria, and calculated values.

Index	NMSE	FB	R
Ideal value	0	0	1
Criterion	<1.5	[-0.3, 0.3]	>0.8
Value	0.2052	0.0399	0.6145

separately. The wind speed and temperature at the inlet of the upwind fetch section are set to be uniform ($U = 1.5$ m/s and $T = 300$ K, respectively). After the flow field reaches a statistically steady state, the mean and turbulence wind profiles and mean temperature profile are collected at a plane near the outlet of the upwind fetch section (coloured in green in Fig. 9a), which aim to serve the inflow conditions of the test section. At the inlet of the test section, the turbulence is generated by the DSRFG method according to the collected turbulence profiles, and the temperature fluctuation is excluded, which is the same as the inflow settings in the main simulations.

After the flow field in the test section reaches a statistically steady state, the profiles of mean streamwise wind speed and temperature at the location of probes (denoted in Fig. 9a) are extracted, and the comparisons are shown in Fig. 9 (b) and (c). It is observed that the simulations properly capture the trends of the profiles under different stratifications, and the discrepancies between the numerical predictions and wind tunnel test results are acceptable. The diabatic CFD model used in this study is thus validated.

4. Air ventilation and thermal stress assessment criteria

4.1. Urban ventilation criteria

Wind velocity ratio (VR) is a popular index to evaluate the air ventilation condition in a real urban site (e.g. Refs. [29,54]), which is defined as:

$$VR = \frac{\bar{u}_p}{\bar{u}_\infty} \quad (19)$$

where \bar{u}_p and \bar{u}_∞ are the mean wind speeds at the pedestrian-level height and boundary layer height, respectively. The boundary layer height indicates the height where wind speed is free from the ground roughness. This study takes the boundary layer height to be 500 m [44], which is two times the height of the tallest building (250 m) in the selected site.

The air ventilation condition in the target site is evaluated by comparing the obtained VR and AVA criterion proposed by Zhang et al. [55] which categorizes the pedestrian-level air ventilation condition into four levels based on the prevailing wind conditions in Hong Kong. The relationship between VR and corresponding air ventilation level are listed in Table 3.

4.2. Thermal stresses criteria

In addition to the air ventilation condition at the pedestrian-level height, thermal stress is another important index for a liveable city that can be influenced by atmospheric stability. This study chooses Universal Thermal Climate Index (UTCI) to assess outdoor thermal stress. Compared with other prevalent thermal stresses criteria, UTCI shows a high sensitivity to the environmental variables under a wide range of climatic conditions [56]. The UTCI criterion quantifies thermal stress by a biometeorological index “equivalent temperature” with a combined consideration of wind speed, relative humidity, air temperature, and mean radiant temperature (T_{mrt}). T_{mrt} is used to quantify the radiant energy transfer between a human body and the surroundings. T_{mrt} is related to the weighted sum of long-wave and short-wave to which the human body is exposed. Accurate evaluation of T_{mrt} in an urban site is complicated and should consider several human and environmental factors [57]. As an accurate estimation of T_{mrt} is not the object of this study, T_{mrt} is set to be 35 °C based on a field observation study in Hong Kong by Lai et al. [57]. The humidity is set to be 80% according to Weerasuriya et al. [30]. The wind speeds and air temperatures will be extracted from the CFD simulations. The UTCI calculator is available online (<http://www.utci.org/>), and the details of correspondence between the UTCI equivalent temperature and thermal stress levels are listed in Table 4.

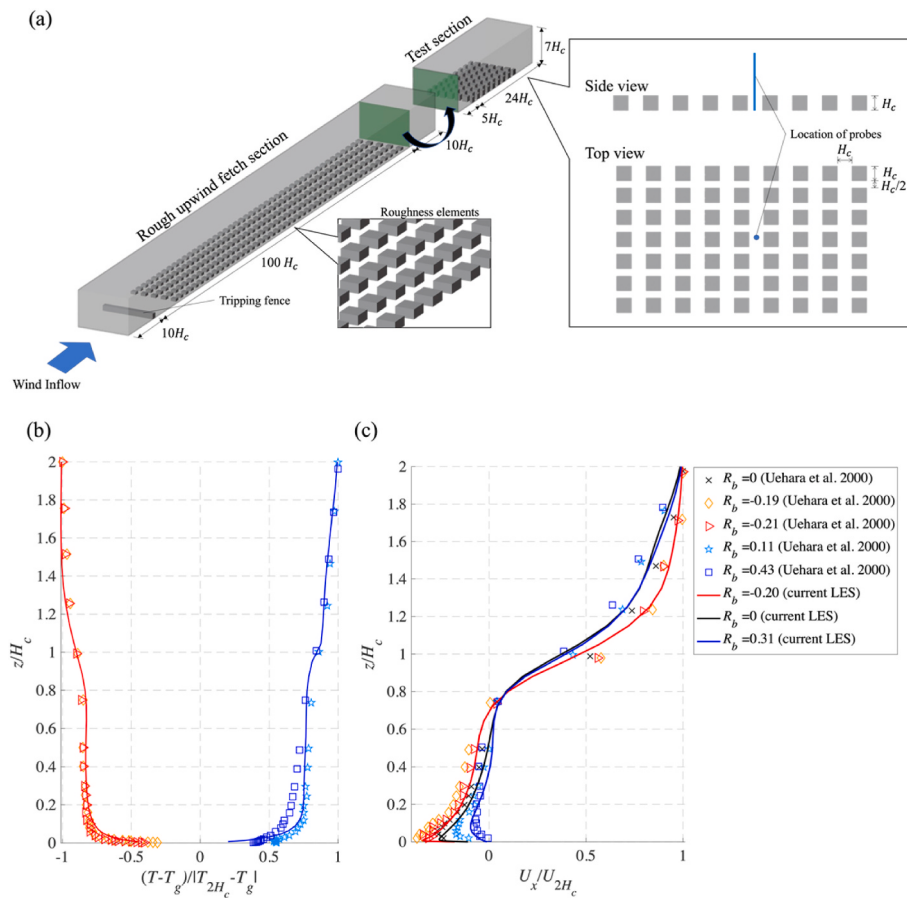


Fig. 9. (a) Models of wind tunnel test and validation about mean profiles of (b) temperature (T_g is the temperature of the ground) and (c) streamwise wind speed under different stratifications.

Table 3
Wind speed criteria.

Wind speed	Corresponding VR	Air ventilation level
<1.6 m/s	<0.56	Low wind speed
1.6–3.5 m/s	0.56–1.21	Acceptable wind speed
3.5–5 m/s	1.21–1.74	High wind speed
>5 m/s	>1.74	Unacceptable wind speed

Table 4
UTCI equivalent temperatures and the corresponding thermal stress level.

UTCI equivalent temperature range (°C)	Thermal stress level
> + 46	Extreme heat stress
+38 to + 46	Very strong heat stress
+32 to +38	Strong heat stress
+26 to +32	Moderate heat stress
+9 to 0	No thermal stress
0 to -13	Slight cold stress
-13 to -27	Strong cold stress
-27 to -40	Very strong cold stress
< -40	Extreme cold stress

5. Results

5.1. Contours of air ventilation and thermal stress

5.1.1. Air ventilation

Fig. 10 (a) – (c) depict the contours of VR under different atmospheric stability conditions. It is found that the neutral case (Fig. 10b)

shows the worst air ventilation, in which the site is covered by a large portion of low wind speed areas ($VR < 0.56$), and there are no high wind speed areas ($VR > 1.21$). The air ventilations in the stable and unstable cases are both improved, especially in the areas with few buildings, but their wind field patterns departure from each other: The wind field in the stable case (Fig. 10a) resembles the condition in the neutral case, in which striking features of mechanically driven flows are maintained. For example, a clear flow separation can be observed in the west part of the domain. However, the wind field in the unstable case (Fig. 10c) is different from those in the other two cases. It indicates that buoyancy-induced convective circulations have severely influenced the mechanically driven flows. To understand the influence of atmospheric stability on air ventilation more intuitively, Fig. 10 (d)–(f) shows the corresponding areas of different air ventilation level under different stratifications. The neutral case is dominated by low wind speed areas which occupy more than 75% of the total area, and 14% and 30% reductions in low wind speed areas are found in the stable and unstable cases, respectively.

To investigate the mechanisms about the influence of atmospheric stability on air ventilation, the time-averaged streamlines of wind flow in x - z cut plane crossing through the geometric centre of the selected urban site are shown in Fig. 11, and the figures are coloured by vertical wind speeds. Compared to the neutral case (Fig. 11b), noticeable downdrafts of the streamlines are observed in the stable case (Fig. 11a). For instance, after the wind flows are interrupted by the tallest building at the centre of the domain, the streamlines are quickly dragged downward after an apparent flow separation. The cause of the downdrafts is that cold air near the ground is uplifted to a higher altitude due to flow separation. As the density of cold air is greater than that of hot air aloft, cold air quickly falls back and result in downdrafts. The

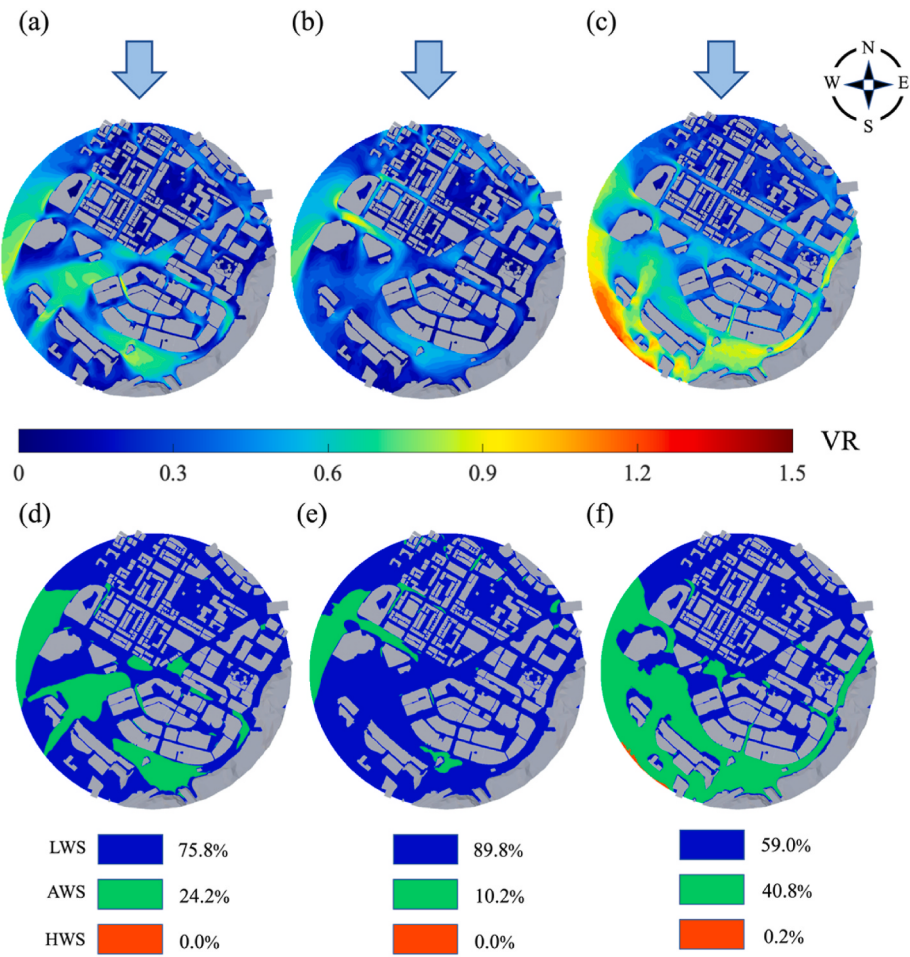


Fig. 10. Contours of VR (upper panels) and air ventilation level at the pedestrian-level height under (a) (d) stable, (b) (e) neutral, and (c) (f) unstable stratification. Arrows in the upper panels indicate wind direction. Labels “LWS”, “AWS”, and “HWS” in the lower panels represent “low wind speed”, “acceptable wind speed”, and “high wind speed” areas, respectively.

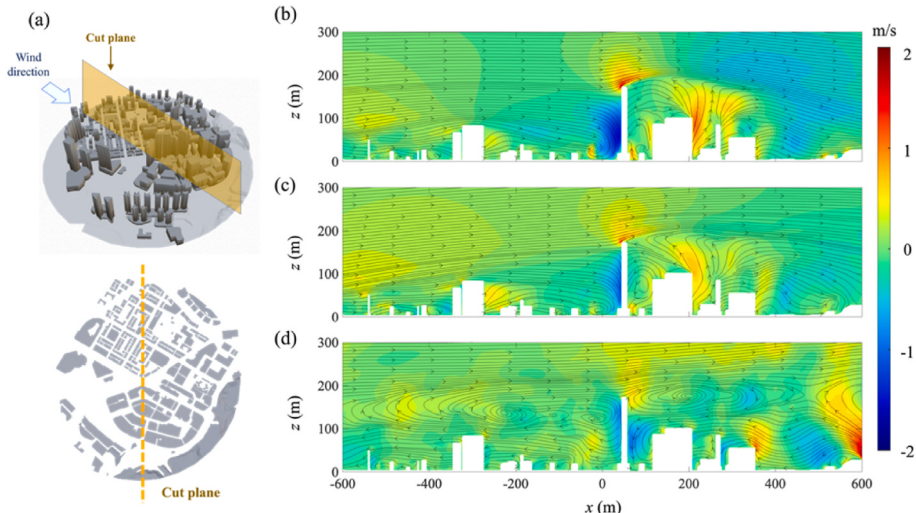


Fig. 11. (a) 3D and vertical view of the cut plane, and time-averaged streamlines on the cut plane under (b) stable, (c) neutral, and (d) unstable stratification.

downdrafts of wind flow may explain the improvement of air ventilation in the stable case as they bring the aloft hot air down to the near-ground level height, which results in a streamwise temperature gradient and sequentially imposes a streamwise buoyance force to push the wind flows.

The condition of the unstable case is more complicated as many large vortex structures are observed due to the buoyancy-induced convective, as shown in Fig. 11 (d). These large vortices destruct the mechanically driven wind fields and greatly enhance the vertical mixing, which strengthens air ventilation at the pedestrian-level height [26,27],

58].

5.1.2. Thermal stress

Fig. 12 (a) – (c) show the contours of UTCI in the selected urban site under different atmospheric stabilities. As Hong Kong's climate is subtropical, it is found that all the obtained UTCI values exceed 26 °C (threshold of moderate heat stress). It is reasonable to postulate that heat stresses and wind speeds are negatively correlated. Hence, it is not surprising that the unstable case, which has the best general air ventilation condition, shows the lowest thermal stress. The UTCI contours in the stable and neutral cases are generally similar, but the stable case shows stronger heat stress areas at the south end of the site, which should be attributed to the dragging down of hot air caused by the aforementioned downdrafts of wind flow.

To further understand the relationship between atmospheric stability and thermal stress, **Fig. 12** (b)–(d) depict the corresponding areas of different thermal stress level under different atmospheric stabilities. The neutral case shows the strongest thermal discomfort with 44% areas of strong heat stress. They are alleviated in the stable and unstable cases, in which an 8% and 32% reduction of strong heat stress areas are observed, respectively. The reductions in strong heat stress areas are similar to the reduction scenarios of low wind speed areas in the air ventilation (14% and 30%, respectively), which proves an inner connection between air ventilation and thermal stress.

5.2. Area of air ventilation and thermal stress level

To quantify the influence of atmospheric stability on air ventilation, the area percentages of VR under different atmospheric stabilities are calculated, as shown in **Fig. 13** (a). Even though the air ventilation is

generally improved under stable stratification, the areas of stagnant wind speed are similar to those in the neutral case ($VR < 0.1$), and the maximum VR in the stable case and neutral case is also the same (around 0.9). On the other hand, the areas of stagnant wind speed are significantly decreased in the unstable case, and the maximum VR is increased to 1.2.

Fig. 13 (b) depicts the area percentages of UTCI under different atmospheric stabilities. It shows that a large portion of values are concentrated near $UTCI = 32^\circ\text{C}$, indicating that the thermal environment at the selected site is generally at the critical point of moderate heat stress and strong heat stress. Therefore, the influence of atmospheric stability can be significant in evaluating the local thermal stress level. The unstable case shows the most significant deviation, in which the curve shifts towards the left with larger areas of low UTCI values. The curves of the stable and neutral cases are similar except for some differences near the cutoff point of moderate heat stress and strong heat stress.

5.3. Urban morphology on air ventilation and thermal stresses

5.3.1. Urban geometry indices

Urban air ventilation and thermal stress are considered to be related to urban morphology (e.g., Refs. [59,60]). Therefore, their relationships under different atmospheric stabilities are examined in this section. The selected site is divided into a series of sub-areas with horizontal dimensions of $50\text{ m} \times 50\text{ m}$ and a height of 300 m, as shown in **Fig. 14** (a) and (b). The morphologies of the buildings in each sub-area can be described by urban geometry indices. This study uses two urban geometry indices: frontal area ratio (λ_f) and ground coverage ratio (λ_g). Similar indices have been adopted in previous AVA studies for street

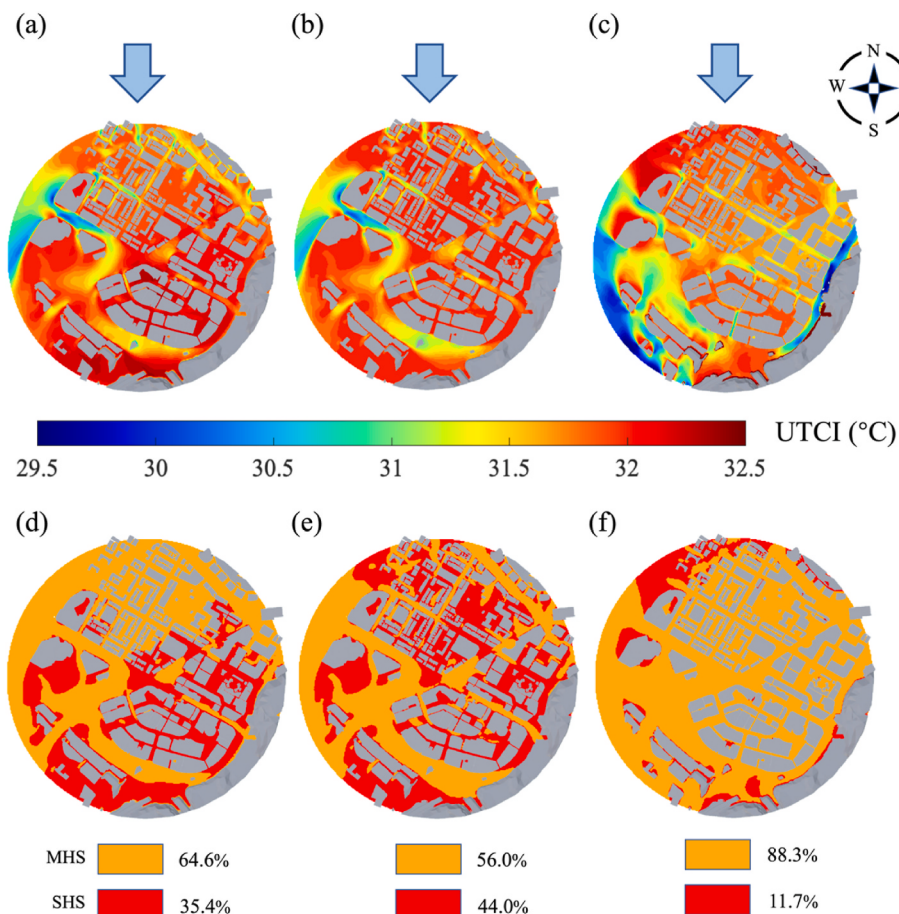


Fig. 12. As in **Fig. 10** but for UTCI. Labels "MHS" and "SHS" represent "moderate heat stress" and "strong heat stress" areas, respectively.

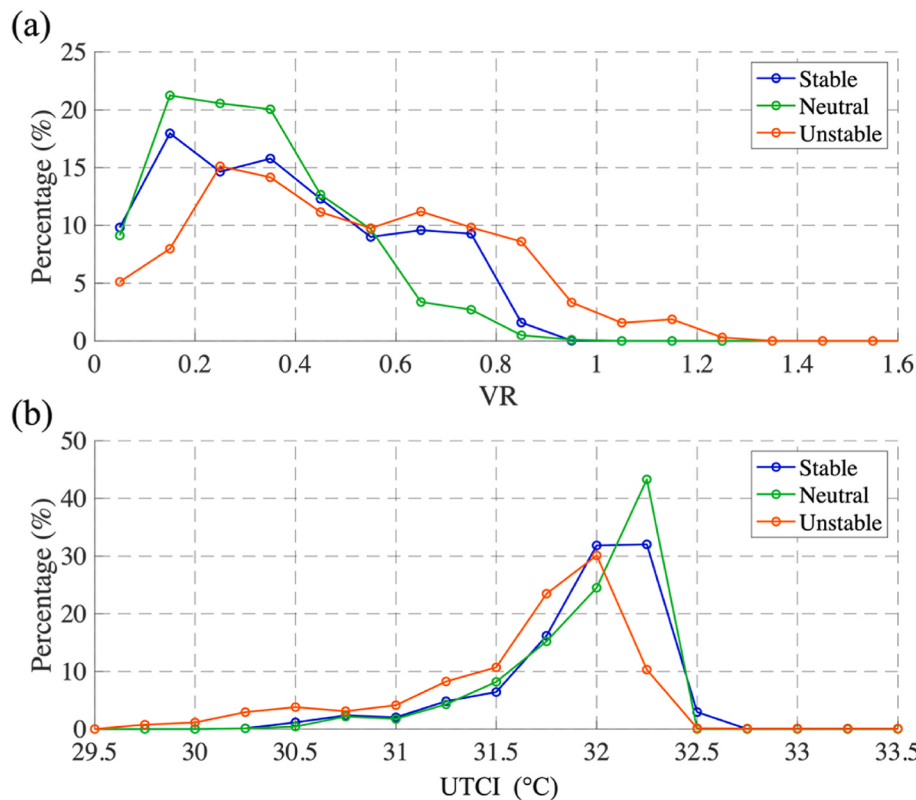


Fig. 13. Area percentages of (a) VR and (b) UTCI under different atmospheric stability conditions.

canyons [15,61] and real urban sites (e.g., Refs. [18,26,27]). λ_f is calculated by a ratio of the streamwise projection area of buildings to the frontal area, and λ_g is calculated by a ratio of the vertical projection area of buildings to the ground area (The above-mentioned terminologies are marked in Fig. 14b). Higher values of λ_f and λ_g indicate a more compact urban configuration. Fig. 14 (c) and (d) show the calculated λ_g and λ_f , respectively, in each sub-area. It is observed that they are to some degree correlated but not equivalent. The reason is that though both indices describe urban density, λ_g reflects the urban density from the top view, and λ_f is based on the front view.

The relationships between VR and two urban geometry indices are shown in the upper six panels in Fig. 15. Those areas without buildings are not considered in the analyses. As expected, VR negatively correlates to λ_g , and the correlation is the lowest in the unstable case. The possible cause is that the buoyancy-induced strong convection flows and wind direction variations weaken the influence of urban configuration on air ventilation. However, there is no necessary relationship between VR and λ_f as the slopes of the regression lines are zero. This observation may be counterintuitive as previous studies revealed the relationship between building height and nearby wind speeds when the building is isolated [62] or surrounded by idealized street canyons [40]. Gronemeier et al. [26] attributed it to that the building layout in a real urban site is not ideally aligned, and the irregular building layouts destruct the wind field that is observed in idealized configuration.

The lower six panels in Fig. 15 show the relationships between the two urban geometry indices and UTCI under different atmospheric stabilities. The correlations between the UTCI values and λ_g are lower than those related to VR because thermal stress is driven by a more complicated process pertinent to the combined effects of environmental factors. However, as air ventilation and heat stress are negatively correlated (Section 5.1.2), it is not surprising to observe that the UTCI values increase with λ_g , and the unstable case shows the lowest correlation. Similar to the condition of VR, λ_f does not show an obvious influence on the UTCI value, and the regression lines are almost horizontal. The

above findings somewhat indicate that λ_g is a more important indicator than λ_f in urban planning for improving urban air ventilation and alleviating heat stress.

6. Discussion

This study comprehensively evaluates the influence of atmospheric stability on the urban wind and thermal environment in a real compact urban site in Hong Kong. The novelty of this study is that: First, this paper comprehensively analyses the errors caused by the assumption of neutral atmosphere in the current AVA methodology in evaluating urban air ventilation, which aims to provide a reference to supplement or improve the current AVA methodology. Second, both air ventilation and thermal environment are investigated based on LES in a real compact urban region, while most previous studies only focused on one factor (air ventilation or thermal stress) or were based on an idealized urban layout. Third, most previous studies related to urban wind environment focused on wind-induced discomfort or safety to pedestrians under strong wind conditions. Their findings are generally not applicable to AVA in a compact urban area under weak wind condition. It should be mentioned that AVA hasn't gotten much attention in other metropolises except Hong Kong. This paper provides a framework for evaluating air ventilation and thermal environments in a compact urban region characterised by weak wind condition. Fourth, the relationship between urban morphology and local air ventilation and thermal environment is presented and discussed, which provides useful information for urban planning and renovation in subtropical cities.

This paper aims to provide a methodology and give a qualitative discussion about the influence of atmospheric stability on air ventilation and thermal stress. This study doesn't consider wind flows with different incident wind directions corresponding to different occurrence probabilities. Future studies should consider this factor for a more comprehensive and accurate assessment.

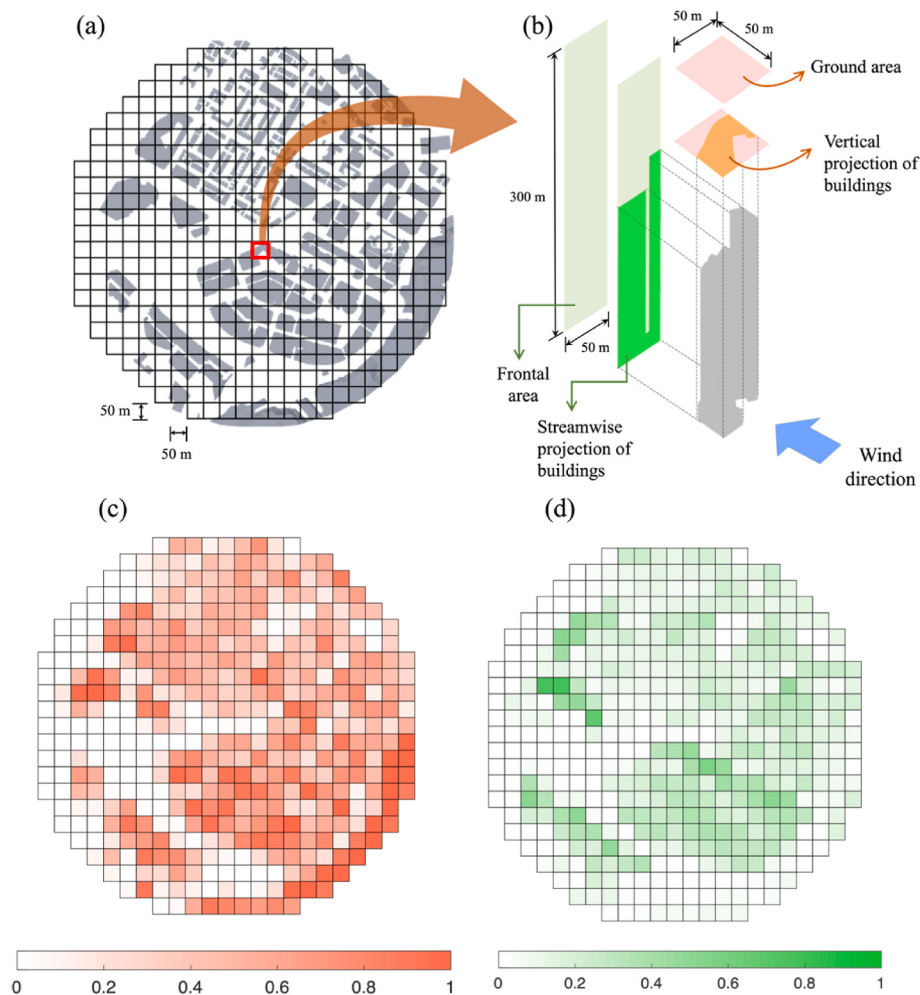


Fig. 14. (a) Division of the urban site, and an example is given in (b) to define ground area, frontal area, streamwise and vertical projection of buildings. (c) and (d) show λ_g and λ_f for all sub-areas, respectively.

7. Conclusion

Given that the current AVA methodology is based on the assumption of neutral atmosphere, this paper investigated the influence of atmospheric stabilities on air ventilation and thermal stress in an urban area. A real compact urban site in Hong Kong was selected for the case study by LES, and the atmospheric stability-induced buoyancy forces were modelled using the Boussinesq approximation. The field observations of equivalent potential temperature profiles in the recent five years were analysed, and they were used to specify the vertical profiles of equivalent potential temperature in the simulations for the stable and unstable cases. The CFD model was validated against the results of a wind tunnel test, and a reasonable agreement was observed. The air ventilation and thermal stress were quantified by wind speed ratio (VR) and Universal Thermal Climate Index (UTCI) equivalent temperature. By detailed comparative study, the major findings are listed as follows:

- Both stable and unstable conditions increase VR at the pedestrian-level height, but the mechanisms are different. For the stable case, hot air is pulled down as wind flows are downdraft, which results in a streamwise temperature gradient at the pedestrian-level height to accelerate air flows. For the unstable case, the flow field is dominated by buoyance-induced convections instead of mechanically driven wind flows, and the increased VR is attributed to enhanced mixing and convective air circulations. The unstable case

shows the best air ventilation in terms of the smallest areas of low wind speed region.

- The calculated UTCI values showed that the selected site is dominated by moderate heat stress and strong heat stress as the climate of Hong Kong is subtropical. Due to the inner connection between air ventilation and thermal stress, the thermal stress is found to be alleviated under stable and unstable stratifications in terms of smaller areas of strong heat stress, and the unstable case shows the lowest thermal stress.
- The influence of urban morphology on air ventilation and thermal stress was investigated. It is found that the ground coverage ratio is negatively and positively proportional to VR and UTCI value, respectively, and the correlations are lower in the unstable case. On the other hand, neither VR nor UTCI value has an obvious relationship with the frontal area ratio. These observations indicate that the ground coverage ratio is a more important design index in urban planning.

CRediT authorship contribution statement

Bin Lu: Writing – original draft, Methodology, Investigation.
Qiusheng Li: Writing – review & editing, Resources, Conceptualization.

Declaration of competing interest

The authors declare that they have no known competing financial

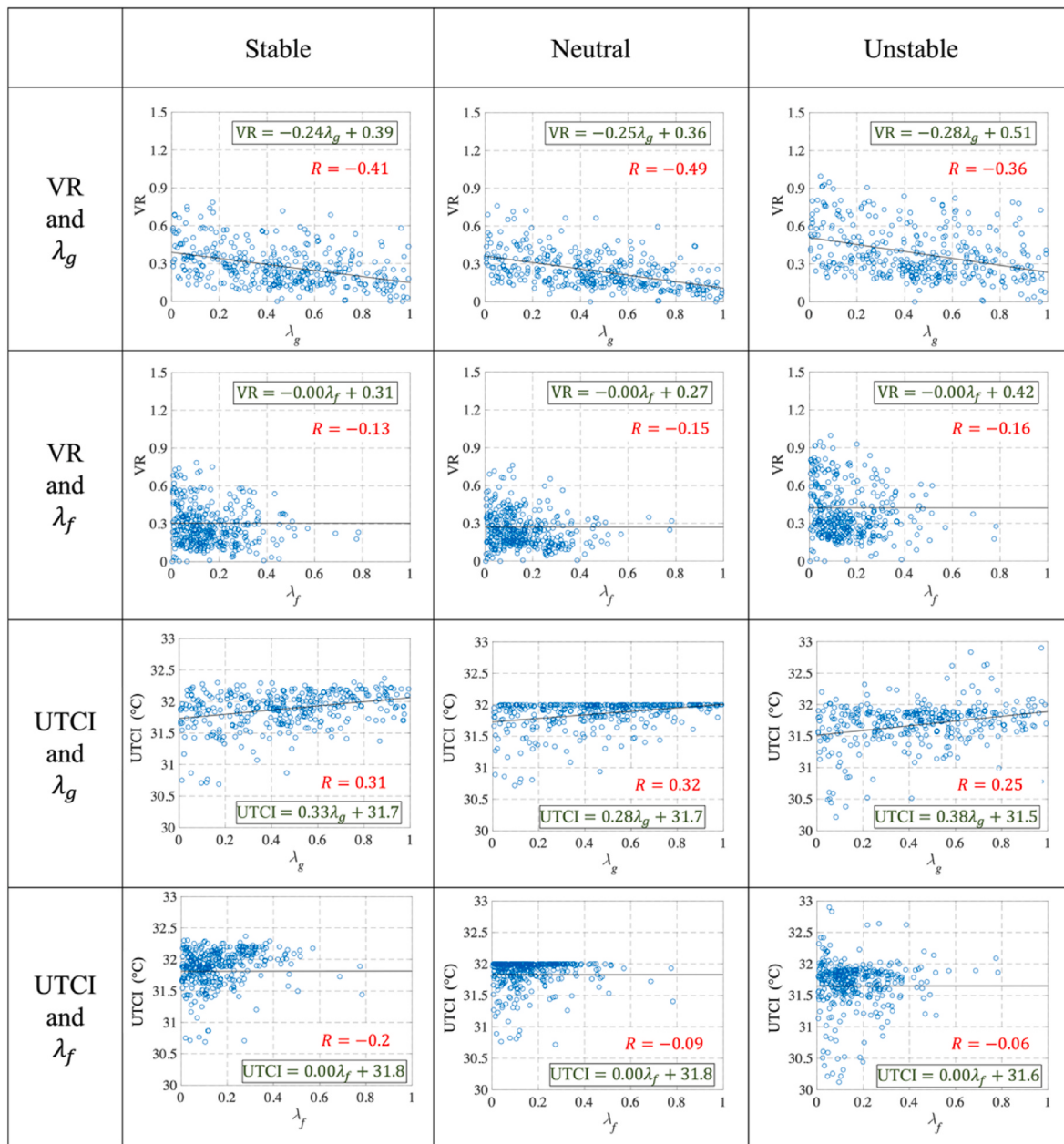


Fig. 15. Relationship between urban geometry indices and wind and thermal environment in the target site under different stratifications.

interests or personal relationships that could have appeared to influence the work reported in this paper.

Acknowledgements

The computational work reported in this paper was carried out using the computational facilities, CityU Burgundy, managed and provided by the Computing Services Centre at City University of Hong Kong. The work described in this paper was fully supported by research grants of City University of Hong Kong (Project No: 9667218 and 9667277).

References

- [1] S. Ye, The land resource and landuse of Hong Kong, *Chin. Geogr. Sci.* 8 (1) (1998) 12–24.
- [2] P. Wang, W.B. Goggins, Y. Shi, X. Zhang, C. Ren, K. Ka-Lun Lau, Long-term association between urban air ventilation and mortality in Hong Kong, *Environ. Res.* 197 (2021) 111000.
- [3] E.P.H. Choi, B.P.H. Hui, E.Y.F. Wan, Depression and anxiety in Hong Kong during COVID-19, *Int. J. Environ. Res. Publ. Health* 17 (10) (2020) 3740.
- [4] L. Morawska, J. Cao, Airborne transmission of SARS-CoV-2: the world should face the reality, *Environ. Int.* 139 (2020) 105730.
- [5] I.T.S. Yu, Y. Li, T.W. Wong, W. Tam, A.T. Chan, J.H.W. Lee, D.Y.C. Leung, T. Ho, Evidence of airborne transmission of the severe acute respiratory syndrome virus, *N. Engl. J. Med.* 350 (17) (2004) 1731–1739.
- [6] K.W. Oleson, A. Monaghan, O. Wilhelmi, M. Barlage, N. Brunsell, J. Feddema, L. Hu, D.F. Steinhoff, Interactions between urbanization, heat stress, and climate change, *Climatic Change* 129 (3) (2015) 525–541.
- [7] A. Afkaki, M. Mirnezhad, A. Ghaffarianhoseini, A. Ghaffarianhoseini, H. Omrany, Z. H. Wang, H. Akbari, Urban heat island mitigation strategies: a state-of-the-art review on Kuala Lumpur, Singapore and Hong Kong, *Cities* 62 (2017) 131–145.
- [8] E. Ng, V. Cheng, Urban human thermal comfort in hot and humid Hong Kong, *Energy Build.* 55 (2012) 51–65.
- [9] S. Conti, P. Meli, G. Minelli, R. Solimini, V. Toccaceli, M. Vichi, C. Beltrano, L. Perini, Epidemiologic study of mortality during the Summer 2003 heat wave in Italy, *Environ. Res.* 98 (3) (2005) 390–399, 2005.
- [10] E.Y.Y. Chan, W.B. Goggins, J.J. Kim, S.M. Griffiths, A study of intracity variation of temperature-related mortality and socioeconomic status among the Chinese population in Hong Kong, *J. Epidemiol. Community Health* 66 (4) (2012) 322–327.
- [11] R.E. Britter, S.R. Hanna, Flow and dispersion in urban areas, *Annu. Rev. Fluid Mech.* 35 (1) (2003) 469–496.

- [12] X. Li, C. Liu, D. Leung, Development of a model for the determination of air exchange rates for street canyons, *Atmos. Environ.* 39 (38) (2005) 7285–7296.
- [13] C. Liu, D. Leung, M. Barth, On the prediction of air and pollutant exchange rates in street canyons of different aspect ratios using large-eddy simulation, *Atmos. Environ.* 39 (9) (2005) 1567–1574.
- [14] J. Hang, Y. Li, Age of air and air exchange efficiency in high-rise urban areas and its link to pollutant dilution, *Atmos. Environ.* 45 (31) (2011) 5572–5585.
- [15] R. Ramponi, B. Blocken, L.B. de Coo, W.D. Janssen, CFD simulation of outdoor ventilation of generic urban configurations with different urban densities and equal and unequal street widths, *Build. Environ.* 92 (2015) 152–166.
- [16] J. Hang, M. Sandberg, Y. Li, Effect of urban morphology on wind condition in idealized city models, *Atmos. Environ.* 43 (4) (2009) 869–878.
- [17] B. Blocken, J. Persoon, Pedestrian wind comfort around a large football stadium in an urban environment: CFD simulation, validation and application of the new Dutch wind nuisance standard, *J. Wind Eng. Ind. Aerod.* 97 (5–6) (2009) 255–270.
- [18] N. Antoniou, H. Montazeri, H. Wigo, M.K.A. Neophytou, B. Blocken, M. Sandberg, CFD and wind-tunnel analysis of outdoor ventilation in a real compact heterogeneous urban area: evaluation using “air delay”, *Build. Environ.* 126 (2017) 355–372.
- [19] S.J. Mei, C. Yuan, Urban Buoyancy-Driven Air Flow and Modelling Method: A Critical Review, *Building and Environment*, 2021, 108708.
- [20] G. Duan, K. Ngan, Sensitivity of turbulent flow around a 3-D building array to urban boundary-layer stability, *J. Wind Eng. Ind. Aerod.* 193 (2019) 103958.
- [21] G. Duan, K. Ngan, Influence of thermal stability on the ventilation of a 3-D building array, *Build. Environ.* 183 (2020) 106969.
- [22] W.C. Cheng, C.H. Liu, D.Y.C. Leung, On the correlation of air and pollutant exchange for street canyons in combined wind-buoyancy-driven flow, *Atmos. Environ.* 43 (24) (2009) 3682–3690.
- [23] X.X. Li, R.E. Britter, T.Y. Koh, L.K. Norford, C.H. Liu, D. Entekhabi, D.Y.C. Leung, Large-eddy simulation of flow and pollutant transport in urban street canyons with ground heating, *Boundary-Layer Meteorol.* 137 (2) (2010) 187–204.
- [24] W.C. Cheng, C.H. Liu, Large-eddy simulation of turbulent transports in urban street canyons in different thermal stabilities, *J. Wind Eng. Ind. Aerod.* 99 (4) (2011) 434–442.
- [25] L. Yang, Y. Li, Thermal conditions and ventilation in an ideal city model of Hong Kong, *Energy Build.* 43 (5) (2011) 1139–1148.
- [26] T. Gronemeier, S. Raasch, E. Ng, Effects of unstable stratification on ventilation in Hong Kong, *Atmosphere* 8 (12) (2017) 168.
- [27] W. Wang, E. Ng, Air ventilation assessment under unstable atmospheric stratification—a comparative study for Hong Kong, *Build. Environ.* 130 (2018) 1–13.
- [28] A. Nordbo, L. Järvi, S. Haapanala, J. Moilanen, T. Vesala, Intra-city variation in urban morphology and turbulence structure in Helsinki, Finland, *Boundary-Layer Meteorol.* 146 (3) (2013) 469–496.
- [29] W. Zhang, C.M. Mak, Z.T. Ai, W.M. Siu, A study of the ventilation and thermal comfort of the environment surrounding a new university building under construction, *Indoor Built Environ.* 21 (4) (2012) 568–582.
- [30] A.U. Weerasuriya, X. Zhang, B. Lu, K.T. Tse, C.H. Liu, Optimizing lift-up design to maximize pedestrian wind and thermal comfort in ‘hot-calm’ and ‘cold-windy’ climates, *Sustain. Cities Soc.* 58 (2020) 102146.
- [31] J.F. Barlow, Progress in observing and modelling the urban boundary layer, *Urban Clim.* 10 (2014) 216–240.
- [32] A.U. Weerasuriya, K.T. Tse, X. Zhang, K.C.S. Kwok, Integrating twisted wind profiles to Air Ventilation Assessment (AVA): the current status, *Build. Environ.* 135 (2018) 297–307.
- [33] A.U. Weerasuriya, K.T. Tse, X. Zhang, K.C.S. Kwok, Equivalent wind incidence angle method: a new technique to integrate the effects of twisted wind flows to AVA, *Build. Environ.* 139 (2018) 46–57.
- [34] A.U. Weerasuriya, K.T. Tse, X. Zhang, S.W. Li, A wind tunnel study of effects of twisted wind flows on the pedestrian-level wind field in an urban environment, *Build. Environ.* 128 (2018) 225–235.
- [35] S. Zhang, K.C. Kwok, H. Liu, Y. Jiang, K. Dong, B. Wang, A CFD study of wind assessment in urban topology with complex wind flow, *Sustain. Cities Soc.* 71 (2021) 103006.
- [36] F. Bazdidi-Tehrani, S. Masoumi-Verki, P. Gholamalipour, Impact of opening shape on airflow and pollutant dispersion in a wind-driven cross-ventilated model building: large eddy simulation, *Sustain. Cities Soc.* 61 (2020) 102196.
- [37] X. Zheng, J. Yang, CFD simulations of wind flow and pollutant dispersion in a street canyon with traffic flow: comparison between RANS and LES, *Sustain. Cities Soc.* 75 (2021) 103307.
- [38] J.H. Ferziger, M. Perić, R.L. Street, *Computational Methods for Fluid Dynamics*, Springer International Publishing, Berlin, 2002.
- [39] X. Zhang, A.U. Weerasuriya, B. Lu, K.T. Tse, C.H. Liu, Y. Tamura, Pedestrian-level wind environment near a super-tall building with unconventional configurations in a regular urban area, *Build. Simulat.* 13 (2) (2020) 439–456.
- [40] X. Zhang, A.U. Weerasuriya, X. Zhang, K.T. Tse, B. Lu, C.Y. Li, C.H. Liu, Pedestrian wind comfort near a super-tall building with various configurations in an urban-like setting, *Build. Simulat.* 13 (6) (2020) 1385–1408.
- [41] Y. Tominaga, A. Mochida, R. Yoshie, H. Kataoka, T. Nozu, M. Yoshikawa, T. Shirasawa, AJI guidelines for practical applications of CFD to pedestrian wind environment around buildings, *J. Wind Eng. Ind. Aerod.* 96 (10–11) (2008) 1749–1761.
- [42] C.S.Y. Cham, K.C.S. Kwok, Terrain characterisation and design wind profiles for Hong Kong, *Trans. Hong Kong Inst. Eng.* 18 (4) (2011) 2–9.
- [43] B. Blocken, J. Carmeliet, T. Stathopoulos, CFD evaluation of wind speed conditions in passages between parallel buildings—effect of wall-function roughness modifications for the atmospheric boundary layer flow, *J. Wind Eng. Ind. Aerod.* 95 (9–11) (2007) 941–962.
- [44] E. Ng, Policies and technical guidelines for urban planning of high-density cities – air ventilation assessment (AVA) of Hong Kong, *Build. Environ.* 44 (7) (2009) 1478–1488.
- [45] GB50009-2012, *Load Code for the Design of Building Structures*, Architecture and Building Press, Beijing, China, 2012.
- [46] AJI-2015, *Recommendations for Loads on Buildings*, Architecture Institute of Japan, Japan, 2015.
- [47] ESDU 85020, *Characteristics of Atmospheric Turbulence Near the Ground—Part II: Single Point Data for Strong Winds (Neutral Atmosphere)*, Engineering Sciences Data Unit, IHS Inc., London, UK, 2001.
- [48] S.H. Huang, Q.S. Li, J.R. Wu, A general inflow turbulence generator for large eddy simulation, *J. Wind Eng. Ind. Aerod.* 98 (10–11) (2010) 600–617.
- [49] A. Pelliccioni, P. Monti, G. Leuzzi, An alternative wind profile formulation for urban areas in neutral conditions, *Environ. Fluid Mech.* 15 (1) (2015) 135–146.
- [50] Y. He, C. Ren, H.W.L. Mak, C. Lin, Z. Wang, J.C.H. Fung, Y.G. Li, A.K.H. Lau, E. Ng, Investigations of high-density urban boundary layer under summer prevailing wind conditions with Doppler LiDAR: a case study in Hong Kong, *Urban Clim.* 38 (2021) 100884.
- [51] M. Korycki, L. Łobocki, A. Wyszogrodzki, Numerical simulation of stratified flow around a tall building of a complex shape, *Environ. Fluid Mech.* 16 (6) (2016) 1143–1171.
- [52] M. Schatzmann, H. Olesen, J. Franke, *COST 732 Model Evaluation Case Studies: Approach and Results*, vol. 123, 2010.
- [53] K. Uehara, S. Murakami, S. Oikawa, S. Wakamatsu, Wind tunnel experiments on how thermal stratification affects flow in and above urban street canyons, *Atmos. Environ.* 34 (10) (2000) 1553–1562.
- [54] W. Wang, E. Ng, Large-eddy simulations of air ventilation in parametric scenarios: comparative studies of urban form and wind direction, *Architect. Sci. Rev.* 61 (4) (2018) 215–225.
- [55] X. Zhang, K.T. Tse, A.U. Weerasuriya, S.W. Li, K.C. Kwok, C.M. Mak, J. Niu, Z. Lin, Evaluation of pedestrian wind comfort near ‘lift-up’ buildings with different aspect ratios and central core modifications, *Build. Environ.* 124 (2017) 245–257.
- [56] K. Blazejczyk, Y. Epstein, G. Jendritzky, H. Staiger, B. Tinz, Comparison of UTCI to selected thermal indices, *Int. J. Biometeorol.* 56 (3) (2012) 515–535.
- [57] A. Lai, M. Maing, E. Ng, Observational studies of mean radiant temperature across different outdoor spaces under shaded conditions in densely built environment, *Build. Environ.* 114 (2017) 397–409.
- [58] W. Wang, X. Wang, E. Ng, The coupled effect of mechanical and thermal conditions on pedestrian-level ventilation in high-rise urban scenarios, *Build. Environ.* 191 (2021) 107586.
- [59] Y. Fang, L. Zhao, Assessing the environmental benefits of urban ventilation corridors: a case study in Hefei, China, *Build. Environ.* 212 (2022) 108810.
- [60] Z. Li, H. Zhang, Y.H. Juan, C.Y. Wen, A.S. Yang, Effects of building setback on thermal comfort and air quality in the street canyon, *Build. Environ.* 208 (2022) 108627.
- [61] M. Shirzadi, P.A. Mirzaei, Y. Tominaga, LES analysis of turbulent fluctuation in cross-ventilation flow in highly-dense urban areas, *J. Wind Eng. Ind. Aerod.* 209 (2021) 104494.
- [62] Y. Tamura, X. Xu, Q. Yang, Characteristics of pedestrian-level mean wind speed around square buildings: effects of height, width, size and approaching flow profile, *J. Wind Eng. Ind. Aerod.* 192 (2019) 74–87.